Stem Cell Reports, Volume *15*

Supplemental Information

Gli1^{+} Cells Couple with Type H Vessels and Are Required for Type H Vessel Formation

Ji Chen, Meng Li, An-Qi Liu, Chen-Xi Zheng, Li-Hui Bao, Kai Chen, Xiao-Lin Xu, Jiang-Tao Guan, Meng Bai, Tao Zhou, Bing-Dong Sui, De-Hua Li, Yan Jin, and Cheng-Hu Hu

Supplemental figures and legends

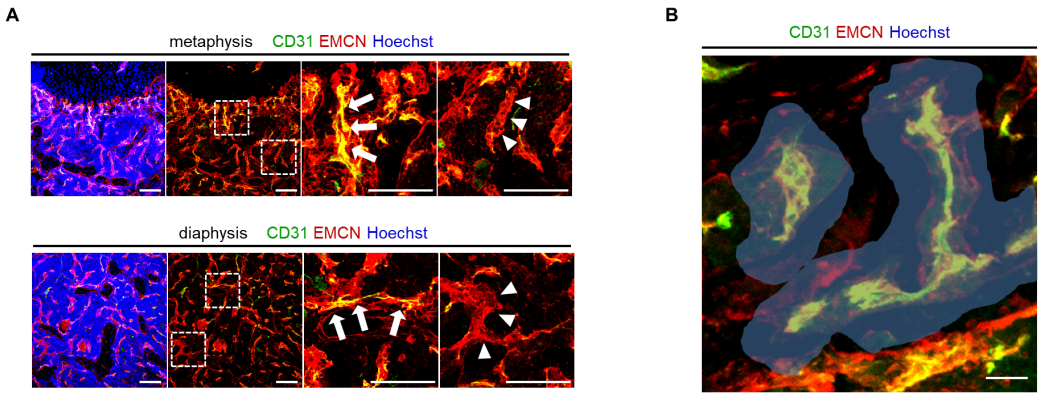

Figure S1. Properties of distinct types of blood vessels in bone and quantification method for adjacent cells. Related to Figure 1.

(A) Representative CD31 (green) and EMCN (red) co-immunostaining images indicating type H vessels (a, $CD31^{hi}EMCN^{hi}$, identified by arrows) and type L vessels (b, $CD31^{lo}EMCN^{lo}$, identified by arrowheads) in femoral metaphysis and diaphysis of mice, counterstained by Hoechst (blue). Boxed area is shown magnified to the right. Scale bars, 100 μm.

(B) Representative CD31 (green) and EMCN (red) co-immunostaining image indicating how the percentages of cells adjacent to specific blood vessels were scored. The fluorescence signals within the grey-masked areas which indicate the region of distance <20 μm around the blood vessels was quantified and regarded as the proteins/markers adjacent to type H or type L vessels. Scale bars, 20 μm.

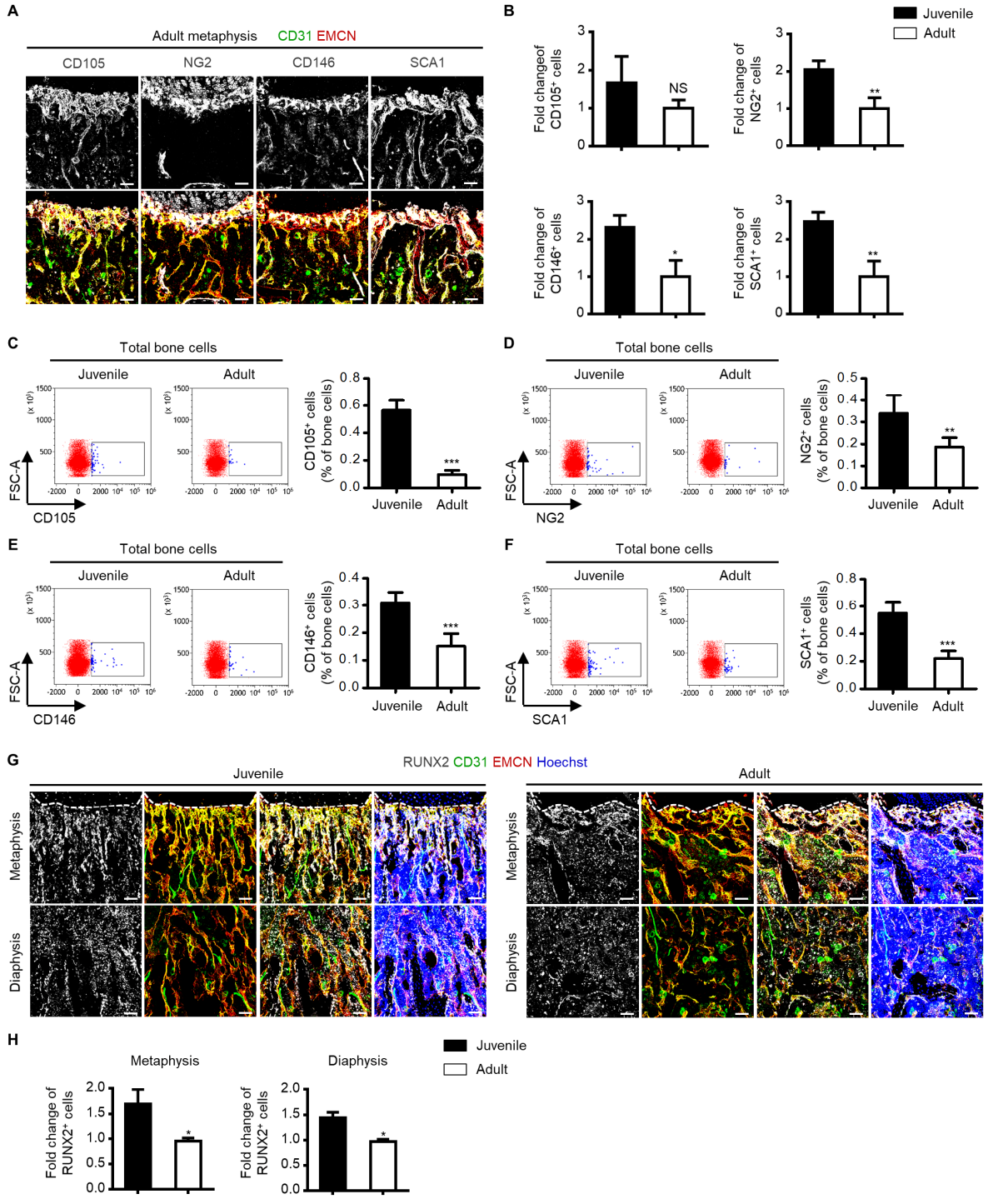

Figure S2. Spatial and Phenotypical Correlation of putative *in vivo* MSC markers and osteoprogenitor marker with Type H Vessels during Bone Growth. Related to Figure 2.

(A) CD31 (green), EMCN (red) and CD105, NG2, CD146 or SCA1 (white) co-immunostaining in femoral metaphysis of adult (8-week old) *Gli1-LacZ* mice. Scale bars, 100 μm.

(B) Quantification of fold changes of $CD105^+$, $NG2^+$, $CD146^+$ and $SCA1^+$ cells in metaphysis of juvenile (4-week old) and adult *Gli1-LacZ* mice. n=3~4 mice per group.

(C-F) Flow cytometric analysis of percentages of $CD105^+$ (C), $NG2^+$ (D), $CD146^+$ (E) and $SCA1^+$ (F) cells in total bone cells of juvenile and adult *Gli1-LacZ* mice. n=4~7 mice per group.

(G) RUNX2 (white), CD31 (green) and EMCN (red) co-immunostaining in femur of juvenile (4-week old) and adult (8-week old) *Gli1-LacZ* mice, counterstained by Hoechst (blue). Dotted lines outline margins of growth plates in metaphysis. Scale bars, 100 μm.

(H) Quantification of fold changes of $RUNX2^+$ cells in metaphysis and diaphysis of juvenile and adult *Gli1-LacZ* mice. n=3 mice per group.

*, $P<0.05$; **, $P<0.01$; ***, $P<0.0001$; NS, $P>0.05$. Data are presented as mean ± SD.

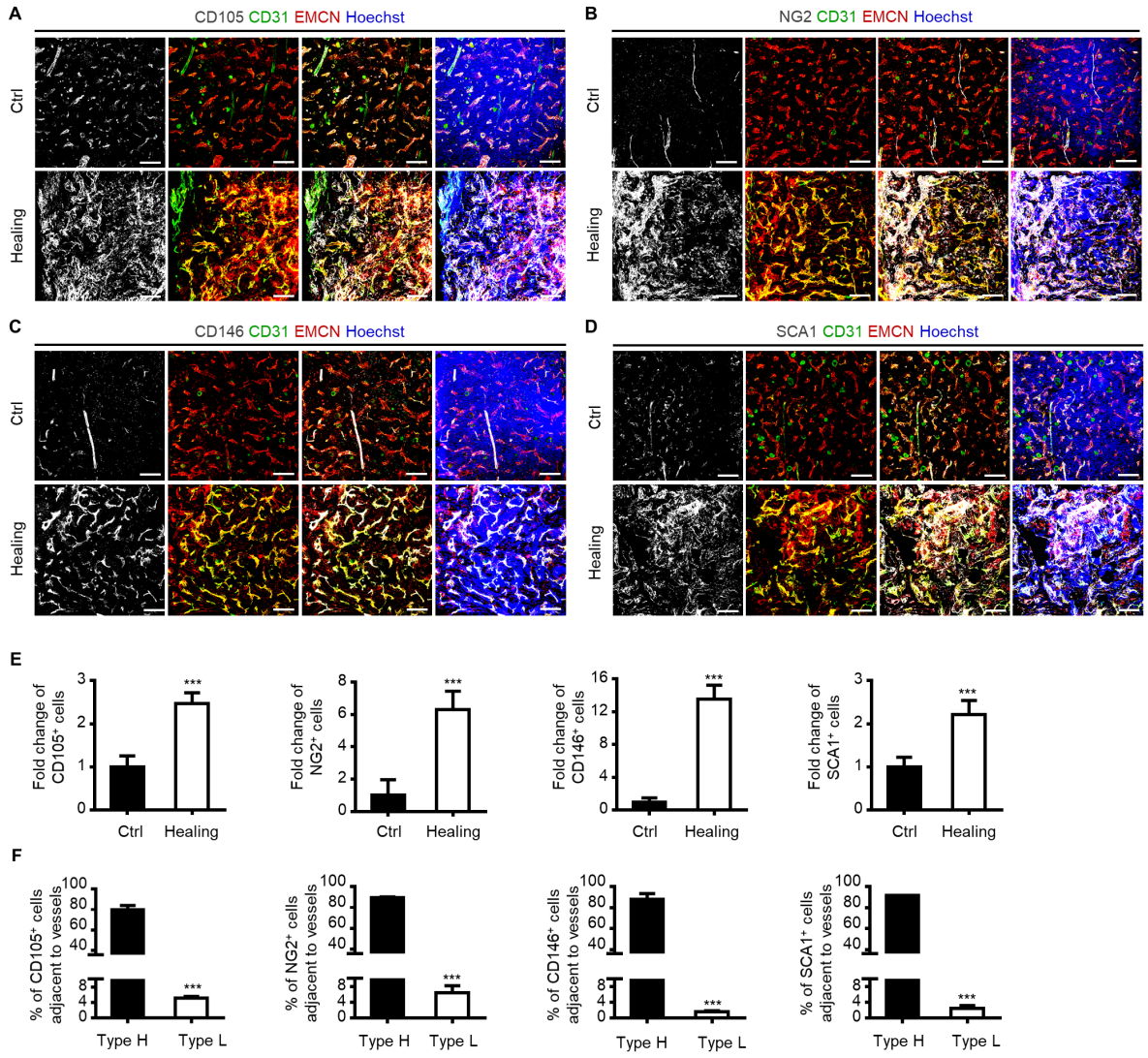

Figure S3. Correlation of MSCs with Type H Vessels in Bone Defect Healing. Related to Figure 3.

(A) CD105 (white), CD31 (green) and EMCN (red) co-immunostaining in femoral diaphysis from 10 week-old *Gli1-LacZ* mice without defects (Ctrl) or with healing defects at 2 weeks after femoral defect modeling, counterstained by Hoechst (blue). Scale bars, 100 μm.

(B) NG2 (white), CD31 (green) and EMCN (red) co-immunostaining in femoral diaphysis from 10 week-old *Gli1-LacZ* mice without defects (Ctrl) or with healing defects at 2 weeks after femoral defect modeling, counterstained by Hoechst (blue). Scale bars, 100 μm.

(C) CD146 (white), CD31 (green) and EMCN (red) co-immunostaining in femoral diaphysis from 10 week-old *Gli1-LacZ* mice without defects (Ctrl) or with healing defects at 2 weeks after femoral defect modeling, counterstained by Hoechst (blue). Scale bars, 100 μm.

(D) SCA1 (white), CD31 (green) and EMCN (red) co-immunostaining in femoral diaphysis from 10 week-old *Gli1-LacZ* mice without defects (Ctrl) or with healing defects at 2 weeks after femoral defect modeling, counterstained by Hoechst (blue). Scale bars, 100 μm.

(E) Quantification of fold changes of $CD105^+$, $NG2^+$, $CD146^+$ and $SCA1^+$ cells in Ctrl and healing area. n=3~6 mice per group.

(F) Quantification of percentages of $CD105^+$, $NG2^+$, $CD146^+$ and $SCA1^+$ cells adjacent to type H and type L

vessels in healing area. n=3 mice per group.

***, $P<0.0001$. Data are presented as mean ± SD.

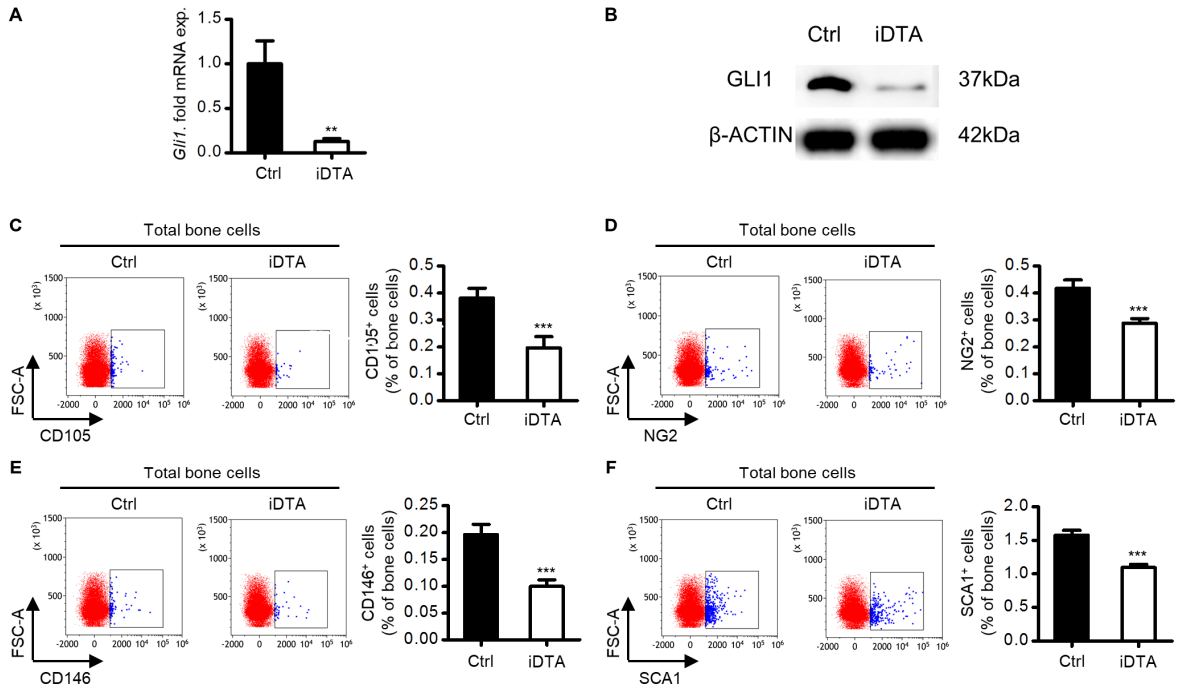

Figure S4. Genetic Ablation of Gli1$^+$ Cells in Bone. Related to Figure 4.

(A) qRT-PCR analysis of *Gli1* mRNA levels in bone tissues of Ctrl and Gli1$^+$ cell ablated mice, indicating ablation of Gli1$^+$ cells. n=3 mice per group.

(B) Western blotting analysis of GLI1 protein levels in bone tissues of Ctrl and Gli1$^+$ cell ablated mice, indicating ablation of Gli1$^+$ cells.

(C-F) Flow cytometric analysis of percentages of CD105$^+$ (A), NG2$^+$ (B), CD146$^+$ (C) and SCA1$^+$ (D) cells in total bone cells of Ctrl and Gli1$^+$ cell ablated mice. n=5 mice per group.

***, P<0.0001. Data are presented as mean ± SD.

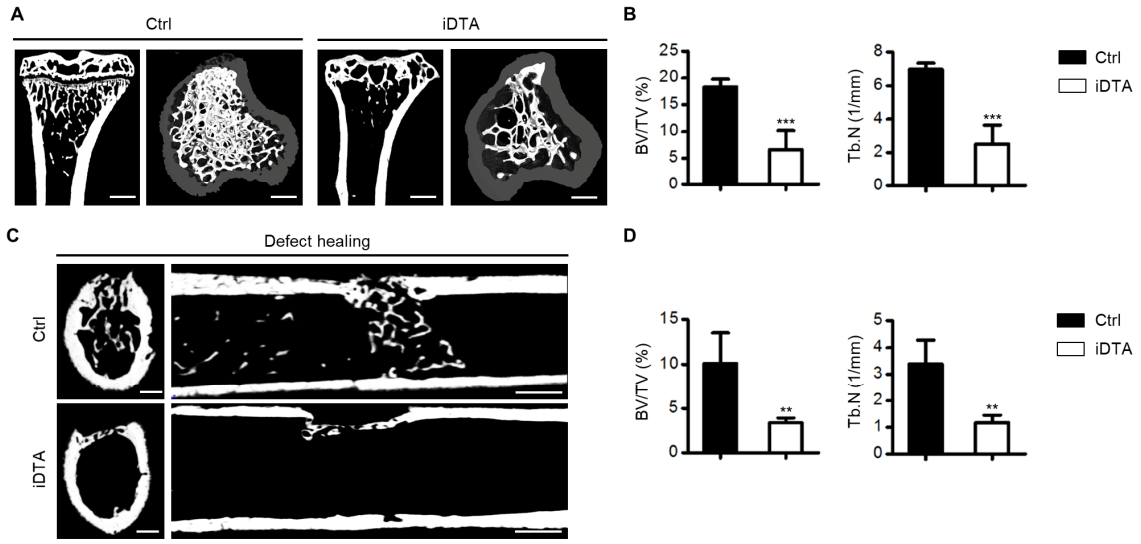

Figure S5. Genetic Ablation of Gli1$^+$ Cells Reduces Bone Mass during Growth and Healing. Related to Figure 4 and Figure 5.

(A) Micro-CT analysis of tibial bone mass in femur of Ctrl and Gli1$^+$ cell ablated mice. Images showing the median sagittal planes and 3-dimensional cross-sectional reconstruction. Scale bars, 500 μm.

(B) Quantification of bone volume and trabecular bone numbers. n=4~5 mice per group.

(C) Micro-CT analysis of defect healing in femur of Ctrl and Gli1$^+$ cell ablated mice. Images showing the median sagittal and coronal planes of healing defects. Scale bars, 200 μm (left) and 500 μm (right).

(D) Quantification of bone volume and trabecular bone numbers. n=4~6 mice per group.

**, P<0.01; ***, P<0.0001. Data are presented as mean ± SD.

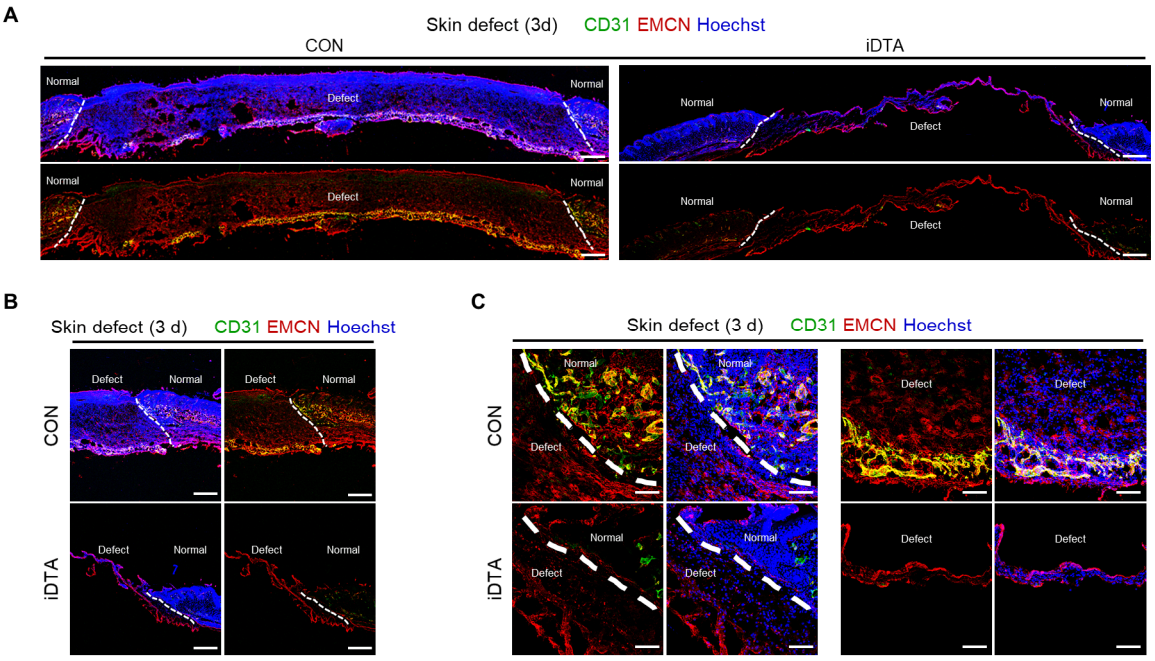

Figure S6. Genetic Ablation of Gli1$^+$ Cells Inhibits Type H Vessel Formation in Skin during Wound Healing. Related to Figure 5.

(A-C) CD31 (green) and EMCN (red) co-immunostaining in skin wound healing area of Ctrl and Gli1$^+$ cell ablated mice, counterstained by Hoechst (blue). Dotted lines outline the boundaries between defect and normal skin. Scale bars, 500 μm (A and B) and 100 μm (C).

Supplemental Experimental Procedures

Primary Cells and Cell Cultures

Total bone cells for flow cytometric analyses (Kusumbe et al., 2014; Schneider et al., 2017) were collected from tibiae and femora after removal of the adherent soft tissues. The hind limb bones were crushed in ice-cold PBS and were digested with collagenase (MP Biomedicals, USA) during incubation at 37°C for 60 min. Single cell suspensions were gathered after washing with PBS and filtration through 200-mesh cell strainers.

Mouse MSCs were isolated from hind limb bone marrow and cultured, as previously described (Lv et al., 2018; Sui et al., 2016; Sui et al., 2018). Briefly, primary mouse bone marrow cells were seeded into culture dishes, incubated overnight, and rinsed with PBS to remove the non-adherent cells. The adherent cells were cultured with alpha-minimum essential medium (α-MEM) supplemented with 20% fetal bovine serum (FBS), 2 mM L-glutamine, 100 U/ml penicillin and 100 g/ml streptomycin (all from Invitrogen, USA) at 37°C in a humidified atmosphere with 5% CO_2. After reaching confluence, MSCs were digested with 0.25% trypsin (MP Biomedicals, USA), passaged, and applied for assays.

Cell Lines

Human umbilical vein endothelial cell (HUVEC) line was purchased from ATCC and was maintained in Dulbecco's modified Eagle medium (DMEM) supplemented with 10% FBS, 2 mM L-glutamine, 100 U/ml penicillin and 100 g/ml streptomycin (all from Invitrogen, USA) at 37°C in a humidified atmosphere of 5% CO_2 (Jing et al., 2017).

Micro-CT Analysis

Freshly dissected hind limb bones were collected and were fixed in 4% PFA (Sigma-Aldrich, USA) solution overnight at 4°C, and were then prepared into 1-cm length specimens. The specimens were scanned at a resolution of 8 μm, a voltage of 80 kV and a current of 80 μA with a desktop micro-CT system (eXplore Locus SP, GE Healthcare, USA) (Sui et al., 2017; Zheng et al., 2018). After 3-dimensional image reconstruction, the region of interest (ROI) was selected in the tibial medial metaphysis or in the femoral defect area. Data were obtained with the VGStudio MAX software (Volume Graphics, Germany) using parameters of BV/TV and Tb.N, as recommended (Bouxsein et al., 2010).

Flow Cytometry

Total primary bone cells were analyzed. For analysis of $Gli1^+$ cells, total bone cells from *Gli1-CreER^{T2};mT/mG* mice were obtained and analyzed after induction of Cre activity by tamoxifen. For analysis of type H ECs, cells were subjected to immunostaining with EMCN antibody (PE-conjugated; sc-65495, Santa Cruz Biotechnology, USA; diluted 1:100) and CD31 antibody (Alexa Fluor 488-conjugated; FAB3628G, R&D Systems, USA; diluted 1:200) for 30 min at 4°C. For analysis of general MSCs, cells were immunostained with antibodies for CD105 (APC-conjugated; 120414, Biolegend, USA; diluted 1:200), NG2 (Alexa Fluor 647-conjugated; sc-53389, Santa Cruz Biotechnology, USA; diluted 1:200), CD146 (APC-conjugated; 134712, Biolegend, USA; diluted 1:100) and SCA1 (APC-conjugated; 108111, Biolegend, USA; diluted 1:200) for 30 min at 4°C. Cells were analyzed with a MoFlo XDP flow cytometer (Beckman Coulter, USA) equipped with the Kaluza software (Beckman Coulter, USA) for quantification (Kusumbe et al., 2014; Schneider et al., 2017).

Tube Formation Assay

As previously described (Xie et al., 2014), Matrigel (BD Biosciences, USA) was plated in 96-well culture plates and incubated at 37°C to polymerize for 45 min. HUVECs (2×10^4 cells/well) or HUVECs with MSCs (1×10^4 cells/well) were seeded onto polymerized Matrigel for 4 h. In indicated experiments, MSCs were pre-treated with

GANT61 (Cayman Chemical, USA), a specific Gli inhibitor (Schneider et al., 2017), DFM (MedChem Express, USA), a HIF-1α stabilizer and activator (Kusumbe et al., 2014), and PX-478 (MedChem Express, USA), a HIF-1α inhibitor (Agarwal et al., 2016), at 10 μM for 48 h. The tube formation of HUVECs was observed under a microscope and the cumulative tube and branching lengths were measured using the ImageJ software.

RNA isolation and qRT-PCR

Total RNA was extracted from bone marrow tissue using Trizol Reagent (Takara, Japan), and complementary DNA (cDNA) was generated using a PrimeScriptTM RT Reagent Kit (Takara, Japan). Then, qRT-PCR was performed with a SYBR Premix Ex Taq II Kit (Takara, Japan) by a Real-Time System (CFX96; Bio-Rad, USA). Quantification was performed by using *Gapdh* as the internal control. The primer sequences used are as follows: *Gli1*, forward 5'-CCAAGCCAACTTTATGTCAGGG-3', reverse 5'-AGCCCGCTTCTTTGTTAATTTGA-3'; *Gapdh*, forward 5'-TGTGTCCGTCGTGGATCTGA-3', reverse 5'-TTGCTGTTGAAGTCGCAGGAG-3'.

Western blotting

Western blotting was performed according to previously studies (Sui et al., 2017; Zhao et al., 2017). Briefly, proteins were extracted from bone marrow tissue and quantified using a BCA Protein Assay kit (TIANGEN, China). Equal amounts of protein samples were loaded onto SDS–PAGE gels, and transferred to polyvinylidene fluoride (PVDF) membranes (Millipore, USA) which were blocked with 5% BSA (Sigma-Aldrich, USA) in TBS for 2 h at room temperature. Then, the membranes were incubated overnight at 4℃ with the following primary antibodies: anti-GLI1 (TA309673, OriGene, USA) and anti-β-ACTIN (ab6276, Abcam, UK). The membranes were washed with TBS containing 0.1% Tween-20 and incubated with peroxidase-conjugated secondary antibodies (Boster, China) for 1 h at room temperature. The protein bands were visualized using an enhanced chemiluminescence kit (Amersham Biosciences, USA) and detected by a gel imaging system (4600; Tanon, China).

Supplemental References

Agarwal, S., Loder, S., Brownley, C., Cholok, D., Mangiavini, L., Li, J., Breuler, C., Sung, H.H., Li, S., Ranganathan, K., et al. (2016). Inhibition of Hif1alpha prevents both trauma-induced and genetic heterotopic ossification. Proceedings of the National Academy of Sciences of the United States of America *113*, E338-347.

Bouxsein, M.L., Boyd, S.K., Christiansen, B.A., Guldberg, R.E., Jepsen, K.J., and Muller, R. (2010). Guidelines for assessment of bone microstructure in rodents using micro-computed tomography. Journal of bone and mineral research : the official journal of the American Society for Bone and Mineral Research *25*, 1468-1486.

Jing, H., Liao, L., Su, X., Shuai, Y., Zhang, X., Deng, Z., and Jin, Y. (2017). Declining histone acetyltransferase GCN5 represses BMSC-mediated angiogenesis during osteoporosis. FASEB journal : official publication of the Federation of American Societies for Experimental Biology *31*, 4422-4433.

Kusumbe, A.P., Ramasamy, S.K., and Adams, R.H. (2014). Coupling of angiogenesis and osteogenesis by a specific vessel subtype in bone. Nature *507*, 323-328.

Lv, Y.J., Yang, Y., Sui, B.D., Hu, C.H., Zhao, P., Liao, L., Chen, J., Zhang, L.Q., Yang, T.T., Zhang, S.F., et al. (2018). Resveratrol counteracts bone loss via mitofilin-mediated osteogenic improvement of mesenchymal stem cells in senescence-accelerated mice. Theranostics *8*, 2387-2406.

Schneider, R.K., Mullally, A., Dugourd, A., Peisker, F., Hoogenboezem, R., Van Strien, P.M.H., Bindels, E.M., Heckl, D., Busche, G., Fleck, D., et al. (2017). Gli1(+) Mesenchymal Stromal Cells Are a Key Driver of Bone Marrow Fibrosis and an Important Cellular Therapeutic Target. Cell stem cell *20*, 785-800 e788.

Sui, B., Hu, C., Liao, L., Chen, Y., Zhang, X., Fu, X., Zheng, C., Li, M., Wu, L., Zhao, X., et al. (2016). Mesenchymal progenitors in osteopenias of diverse pathologies: differential characteristics in the common shift from osteoblastogenesis to adipogenesis. Scientific reports *6*, 30186.

Sui, B.D., Chen, J., Zhang, X.Y., He, T., Zhao, P., Zheng, C.X., Li, M., Hu, C.H., and Jin, Y. (2018). Gender-independent efficacy of mesenchymal stem cell therapy in sex hormone-deficient bone loss via immunosuppression and resident stem cell recovery. Experimental & molecular medicine *50*, 166.

Sui, B.D., Hu, C.H., Zheng, C.X., Shuai, Y., He, X.N., Gao, P.P., Zhao, P., Li, M., Zhang, X.Y., He, T., et al. (2017). Recipient Glycemic Micro-environments Govern Therapeutic Effects of Mesenchymal Stem Cell Infusion on Osteopenia. Theranostics *7*, 1225-1244.

Xie, H., Cui, Z., Wang, L., Xia, Z., Hu, Y., Xian, L., Li, C., Xie, L., Crane, J., Wan, M., et al. (2014). PDGF-BB secreted by preosteoclasts induces angiogenesis during coupling with osteogenesis. Nature medicine *20*, 1270-1278.

Zhao, P., Sui, B.D., Liu, N., Lv, Y.J., Zheng, C.X., Lu, Y.B., Huang, W.T., Zhou, C.H., Chen, J., Pang, D.L., et al. (2017). Anti-aging pharmacology in cutaneous wound healing: effects of metformin, resveratrol, and rapamycin by local application. Aging cell *16*, 1083-1093.

Zheng, C.X., Sui, B.D., Liu, N., Hu, C.H., He, T., Zhang, X.Y., Zhao, P., Chen, J., Xuan, K., and Jin, Y. (2018). Adipose mesenchymal stem cells from osteoporotic donors preserve functionality and modulate systemic inflammatory microenvironment in osteoporotic cytotherapy. Scientific reports *8*, 5215.